

# A comparison of wavelet, ridgelet, and curvelet-based texture classification algorithms in computed tomography

Lucia Dettori\*, Lindsay Semler

*Intelligent Multimedia Processing Laboratory, School of Computer Science, Telecommunications, and Information Systems, DePaul University, 243 S. Wabash Avenue, Chicago, IL 60604, USA*

## Abstract

The research presented in this article is aimed at the development of an automated imaging system for classification of normal tissues in medical images obtained from computed tomography (CT) scans. This article focuses on comparing the discriminating power of several multi-resolution texture analysis techniques using wavelet, ridgelet, and curvelet-based texture descriptors. The approach consists of two steps: automatic extraction of the most discriminative texture features of regions of interest and creation of a classifier that automatically identifies the various tissues. The algorithms are extensively tested and results are compared with standard texture classification algorithms. Tests indicate that using curvelet-based texture features significantly improves the classification of normal tissues in CT scans.

© 2006 Elsevier Ltd. All rights reserved.

**Keywords:** Multi-resolution analysis; Texture classification; Wavelets; Ridgelets; Curvelets; Computed tomography

## 1. Introduction

Over the past several years, 3D imaging equipment has been used more frequently, particularly in the medical field. On a daily basis, hospitals are witnessing a large inflow of digital medical images and related clinical data. This increase in workload has rapidly outpaced the increase in the number of qualified radiologists to navigate, view, and interpret this data. Human analysis and visualization of 3D data received from such machines are often difficult to evaluate due to the quantity of clinical data. Computerized analysis and automated information systems can offer help dealing with the large amounts of data.

The research presented in this article is part of an ongoing project [1–7] aimed at the development of an automated imaging system for classification of tissues in medical images obtained by computed tomography (CT) scans. Classification of human organs in CT scans using shape or gray-level information proves to be a particularly challenging task. This is due

primarily to the changing shape of organs in a stack of slices in 3D medical images and the gray-level intensity overlap in soft tissues. Even so, healthy organs are expected to have a consistent texture within tissues across multiple slices. Therefore, texture analysis of CT scans can be used for classification or segmentation of images based on these textural variations of intensity.

Texture is a commonly used feature in the analysis and interpretation of images. Texture is characterized by a set of local statistical properties of pixel intensities. It measures the variations in an image, looking at properties such as smoothness, coarseness, and regularity. Therefore, the research presented in this article focuses on using texture analysis for the classification of tissues. Traditionally, texture features have been calculated using a variety of statistical, structural, and spectral techniques including co-occurrence matrices [3,8,9], run-length statistics [4], spectral measures, fractal dimensions, statistical moments, and multi-resolution techniques such as wavelets [10], ridgelets [11], and curvelets [12]. Co-occurrence matrices are often used in texture analysis since they are able to capture the spatial dependence of gray-level values within an image. Run-length matrices are able to capture the coarseness of texture in specified directions as defined by gray-level runs. While

\* Corresponding author. Tel.: +1 312 362 8243; fax: +1 312 362 6116.

E-mail addresses: [ldettori@cs.depaul.edu](mailto:ldettori@cs.depaul.edu) (L. Dettori),  
[lsemmler@cs.depaul.edu](mailto:lsemmler@cs.depaul.edu) (L. Semler).

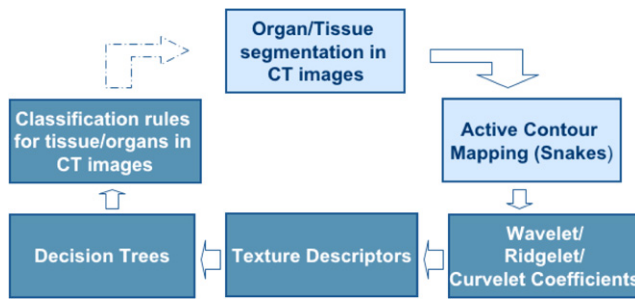


Fig. 1. Methodology diagram.

these texture features are not wavelet based, these techniques are mentioned because they are used for comparison with the wavelet, ridgelet, and curvelet-based techniques proposed in this research.

This research focuses on using multi-resolution texture analysis for the classification of tissues from normal chest and abdomen CT scans. It offers a comprehensive analysis of five forms of multi-resolution analysis, as well as a comparison with two standard texture classification algorithms: co-occurrence and run-length. Texture features were computed from the following multi-resolution transforms: the Haar wavelet [13], Daubechies wavelet [14], Coiflet wavelet [14], ridgelet [15], and curvelet transforms [16].

Multi-resolution analysis [17,25,26] has been successfully used in image processing with the recent emergence of applications to texture classification. Several studies have investigated the discriminating power of wavelet-based features in various applications including: image compression [18], image denoising [19], and classification of natural textures [10]. Recently, the finite ridgelet and curvelet transforms have emerged as a new multi-resolution analysis tool. In recent years, the ridgelet transform has been used in image contrast enhancement and image denoising [20,27]. To the authors' knowledge, applications of ridgelets to texture classification have only been investigated in the context of natural images [11], and curvelet-based applications have been investigated only in image representation of astronomical images [12]. This paper compares texture classification using features derived from the wavelet, ridgelet, and curvelet transforms of CT medical images. Our tests clearly show that curvelet-based features outperform all other multi-resolution techniques, as well as run-length and co-occurrence-based algorithms.

The texture classification algorithm proposed in this article consists of three main steps: segmentation of regions of interest from CT scans, extraction of the most discriminative texture features, and creation of a classifier that automatically identifies the various tissues. The overall goal is to develop a textural model for each texture class in the data set. The general algorithm is summarized in the methodology diagram below (Fig. 1).

The organs were initially segmented to obtain pure samples of each texture; these were used for training the classification algorithm. Using an Active Contour Mapping algorithm, pure tissues were segmented from the original CT scans (Fig. 2).

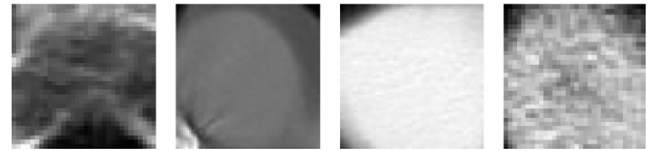


Fig. 2. Example DICOM images (backbone, heart, liver, kidney).

The appropriate multi-resolution transform was applied and a set of texture descriptors was extracted from the transformed image. These features characterized the textural properties of the images and were used to train the classifier to recognize each texture class. The classification step was implemented through a decision tree classifier based on the cross-validation classification and regression tree (C&RT) approach [2]. Given textural features, a decision tree generated a set of rules that were integrated into a classification system. The testing set was then fed through the classification system, resulting in a misclassification matrix from which performance measures were calculated.

The paper is structured as follows: Section 2 describes in more detail the multi-resolution analysis and summarizes the continuous forms of the wavelet, ridgelet, and curvelet transforms. Section 3 discusses the overall methodology, including the discrete forms of the three transforms, as well as the classifier and performance measures. Section 4 presents a comparison of the results.

## 2. Multi-resolution analysis

Multi-resolution analysis [17] allows for the preservation of an image according to certain levels of resolution or blurring. Broadly speaking, multi-resolution analysis allows for the zooming in and out on the underlying texture structure. Therefore, the texture extraction is not affected by the size of the pixel neighborhood. This multi-resolution quality is one of the reasons why wavelets have been useful in so many applications from image compression to image de-noising and edge detection [21].

By decomposing the image into a series of high-pass and low-pass bands, the wavelet transform extracts directional details that capture horizontal, vertical and diagonal activity. However, these three linear directions are limiting, and might not capture enough directional information in noisy images, such as medical CT scans, which do not have strong horizontal, vertical, and diagonal directional elements. Ridgelets, like wavelets, provide multi-resolution texture information; however, they capture structural information of an image based on multiple radial directions in the frequency domain. The multi-directional capabilities of the ridgelet transform provide better texture discrimination than its wavelet counterpart. One limitation to this approach is that ridgelets are most effective in detecting linear radial structures, which also are not dominant in medical images. The curvelet transform is a recent extension of the ridgelet transform; curvelets are proven to be particularly effective at detecting image activity along curves instead of radial directions. Instead of capturing structure along radial lines, the

curvelet transform captures this structural activity along radial ‘wedges’ in the frequency domain.

Since their development in the early 1980s, several wavelet families have emerged. The curvelet, ridgelet, and other such transforms are all extensions of the wavelet transform. This application requires the use of discrete versions of the transforms, which are still the subject of current research. For completeness, the following section contains a brief review of the continuous transforms. The discrete transforms used for texture extraction are described in Section 3.

### 2.1. Wavelets

Three families of wavelets were investigated: Haar (H), Daubechies 4 (D4), and Coiflet (C6) [13,14]. Other related papers used similar wavelet families for comparison [14]. The Haar, Daubechies, and Coiflet families were considered since they differ substantially in the number of adjacent pixels used to extract the wavelet coefficients, from which the texture features are derived. These three were investigated specifically for their increasingly larger filters and smoother windows. Surprisingly, in our application, the Haar wavelet outperforms the Daubechies and Coiflet wavelets.

A wavelet can decompose a signal or an image with a series of averaging and differencing calculations. Wavelets compute average intensity properties as well as several detailed contrast levels distributed throughout the image. Wavelets can be calculated according to various levels of resolution or blurring depending on how many levels of averages are calculated. The general mother wavelet can be constructed from the following scaling  $\phi(x)$  and wavelet functions  $\psi(x)$ :

$$\phi(x) = \sqrt{2} \sum h(k) \phi(2x - k), \quad (1)$$

$$\psi(x) = \sqrt{2} \sum g(k) \phi(2x - k), \quad (2)$$

where  $g(k) = -1^k h(N - 1 - k)$ , and  $N$  is the number of scaling and wavelet coefficients. The sets of scaling ( $h(k)$ ) and wavelet ( $g(k)$ ) function coefficients vary depending on their corresponding wavelet bases. For more details on these wavelet families see, for example [10,13,14,18].

### 2.2. Ridgelet transform

In 1998, Donoho introduced the ridgelet transform [15]. The continuous ridgelet transform (CRT) can be defined from a 1D wavelet function oriented at constant lines and radial directions. The CRT in  $R^2$  is defined by

$$\text{CRT}_f(a, b, \theta) = \int_{R^2} \psi_{a,b,\theta}(x) f(x) dx, \quad (3)$$

where the ridgelets  $\psi_{a,b,\theta}(x)$  in 2D are defined using a wavelet function:

$$\psi_{a,b,\theta}(x) = a^{-1/2} \psi((x_1 \cos \theta + x_2 \sin \theta - b)/a). \quad (4)$$

This is oriented at angles  $\theta$ , and constant along the lines  $x_1 \cos \theta + x_2 \sin \theta = \text{const}$ . For details see Ref. [20]. Essentially,

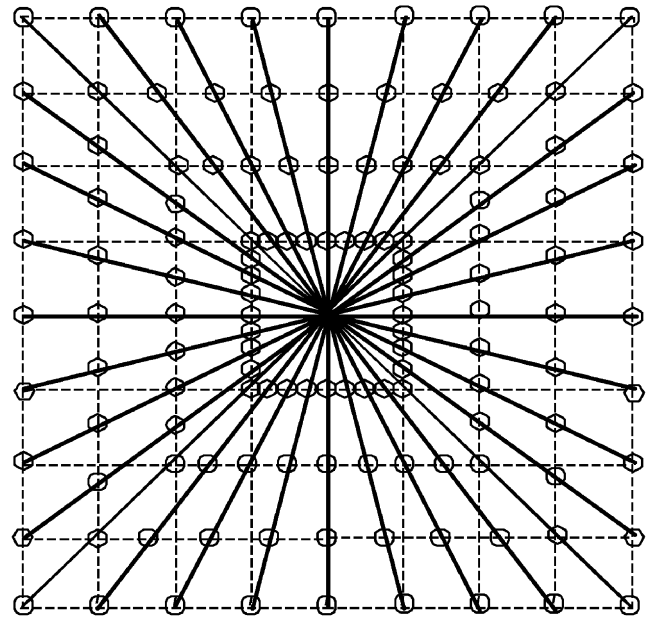


Fig. 3. Illustration of the radial grid of the ridgelet transform.

the ridgelet radial lines are defined by a slope  $\theta$  and an intercept  $b$ . The CRT is similar to the continuous wavelet transform except that point parameters  $(x, y)$  are now replaced by line parameters  $(b, \theta)$ . Fig. 3 illustrates the radial grid.

Generally speaking, wavelets detect objects with point singularities, while ridgelets are able to represent objects with line singularities.

### 2.3. Curvelet transform

In 2000, Candes and Donoho introduced the curvelet transform [22]. The continuous curvelet transform can be defined by a pair of windows  $W(r)$  (a radial window) and  $V(t)$  (an angular window), with variables  $W$  as a frequency-domain variable, and  $r$  and  $\theta$  as polar coordinates in the frequency-domain.

$$\sum_{j=-\infty}^{\infty} W^2(2^j r) = 1, \quad r \in \left(\frac{3}{4}, \frac{3}{2}\right), \quad (5)$$

$$\sum_{l=-\infty}^{\infty} V^2(t - l) = 1, \quad t \in \left(-\frac{1}{2}, \frac{1}{2}\right). \quad (6)$$

A polar ‘wedge’ represented by  $U_j$  is supported by  $W$  and  $V$ , the radial and angular windows.  $U_j$  is defined in the Fourier domain by

$$U_j(r, \theta) = 2^{-3j/4} W(2^{-j} r) V\left(\frac{2^{\lfloor j/2 \rfloor} \theta}{2\pi}\right). \quad (7)$$

The curvelet transform can be defined as a function of  $x = (x_1, x_2)$  at scale  $2^{-j}$ , orientation  $\theta_l$ , and position  $x_k^{(j,l)}$  by

$$\varphi_{j,l,k}(x) = \varphi_j(R_{\theta_l}(x - x_k^{(j,l)})), \quad (8)$$

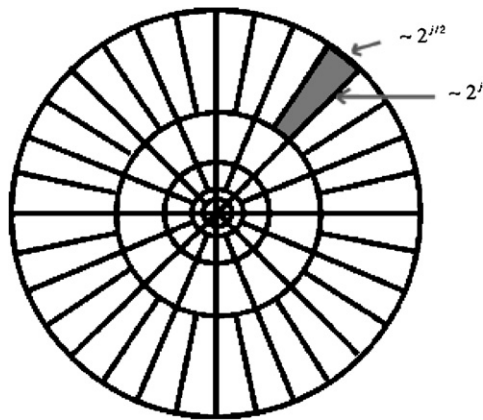


Fig. 4. Curvelet tiling in the frequency domain.

where  $R_\theta$  is the rotation in radians. Fig. 4 illustrates the polar ‘wedges’ represented by  $U_j$ . Further details are presented in Ref. [22].

### 3. Methodology

The texture classification algorithm consists of three main steps: segmentation of regions of interest, extraction of the most discriminative texture features, and creation of a classifier that automatically identifies the various tissues. The following section describes the data set and segmentation process. Section 3.2 describes the finite transforms and the texture extraction methods. Section 3.3 describes the classifier and performance measures used in the classification.

#### 3.1. The data set

The texture classification algorithms were tested on 3D data extracted from two normal chest and abdomen CT studies from Northwestern Memorial Hospital. The data consisted of 340 2D DICOM images, each image being  $512 \times 512$  and having 12-bit gray-level resolution. Ideally, a radiologist would segment the training set in order to have ground truth images to train the classifier. However, since this was not available, the organs were segmented using a supervised Active Contour Models (‘Snake’) algorithm [1]. Five organs were segmented from the initial data: heart, liver, spleen, kidney, and backbone. An Active Contour Model is a function that recreates a boundary given a user-defined starting curve and several parameters. The curve evolves to match the nearest internal boundary depending heavily on gradient intensity measures. The boundary curve can then be used to separate the object from the background [1]. Using this segmentation algorithm, the following slices were generated: 140 backbone, 52 heart, 58 liver, 54 kidney, and 40 spleen. Wavelets, ridgelets, and curvelets are extremely sensitive to contrast in gray-level intensity. Therefore, in order to use wavelet, ridgelet, or curvelet-based texture features, it was necessary to eliminate all background pixels to avoid mistaking the edge between the artificial background and the organ as a texture feature. Each slice was therefore further cropped,

and only square sub-images fully contained in the interior of the segmented area were generated. Fig. 5 shows an example CT scan and a segmented and cropped slice of heart.

These images were  $31 \times 31$  pixels (for ridgelets) or  $32 \times 32$  pixels (for wavelets and curvelets), resulting in 2091 slices of ‘pure’ single-organ tissue (363 backbone, 446 heart, 506 liver, 411 kidney, 364 spleen). These images were cropped to the respective sizes because of size requirements of  $2^n$  for wavelets and a prime size for ridgelets. This data set was split into a training set and a testing set for the cross-validation decision trees described in Section 3.3.

#### 3.2. Feature extraction

Once the medical images were pre-processed as described in Section 3.1, the various transforms were applied, and textural feature vectors were then extracted. The following multi-resolution transforms were applied: the Haar wavelet, Daubechies wavelet, Coiflet wavelet, ridgelet, and curvelet. These transforms were applied using the discrete forms described in the next section. After the transforms were applied, first- and second-order statistics were extracted for use in classification.

##### 3.2.1. Discrete wavelet transform

There are several ways of generating a 2D wavelet transform; this approach used filters as structured in Appendix B. The construction of the digital filters differs mainly in their scaling and wavelet coefficients. Scaling and wavelet function coefficients are characteristic of their particular families; definitions can be found in Appendix C.

The Haar wavelet uses only two scaling and wavelet function coefficients and calculates pair-wise averages and differences. The Haar transform uses non-overlapping windows and reflects changes between adjacent pixel pairs. The Daubechies (D4) transform has four wavelet and scaling coefficients. A weighted average is computed over four pixels, resulting in a smoother transform. With the increase in wavelet and scaling coefficients, the filter constructions allow for overlapping windows, reflecting all changes between pixel intensities and resulting in over-complete information. When applying a discrete wavelet transform containing more than two scaling or wavelet function coefficients, typically either a mirror or periodic extension technique is applied to the filter. One of these extensions must be used due to the size constraints of the digital filter with respect to the image size. For a standard analysis of these techniques see Ref. [23]. In the mirror extension the mean is computed by averaging the mirror values of the last two pixels of the image. With the periodic technique the mean is computed by averaging the last two pixels in the image vector with the first two. Our tests indicated that in general the mirror extension was preferable. Details of the filter structure are presented in Appendix B. The Coiflet wavelet uses six scaling and wavelet function coefficients. The Coiflet wavelet presents the same problem with filter size; the mirror technique was also applied.



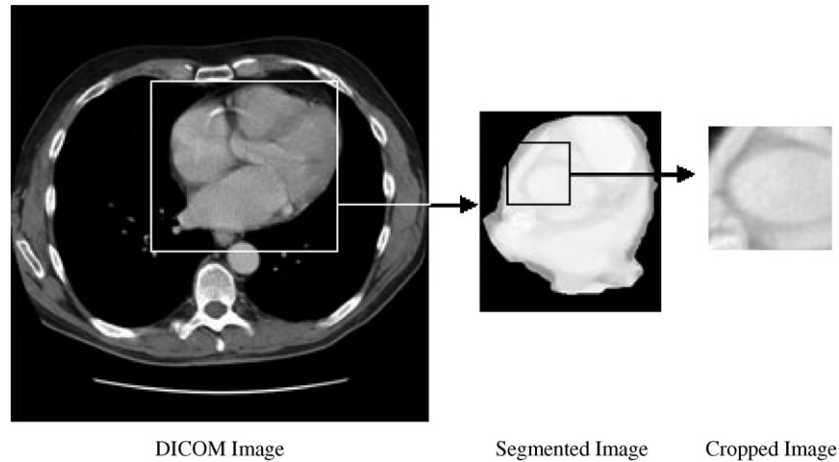


Fig. 5. Sample from CT scan and cropped image from the data set.

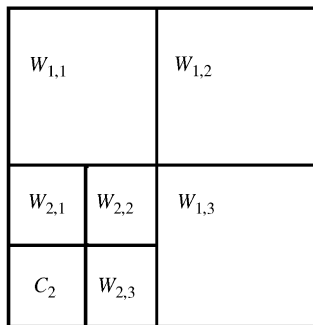


Fig. 6. Wavelet decomposition:  $W_{(\text{resolution}, \text{direction})}$ .

Each of these wavelet filters could be applied multiple times to the averages (see  $C_2$  in Fig. 6), according to the desired level of resolution. In our application, two levels of resolution were extracted for each wavelet. At each resolution level, the wavelet has three detail coefficient matrices representing the vertical, horizontal and diagonal structures of the image.

From each of the detail coefficient matrices  $W$  (see Fig. 6), several first-order and second-order statistics were calculated: mean, standard deviation, energy, entropy, contrast, homogeneity, sum-mean, variance, maximum probability, inverse difference moment, and cluster tendency (see Appendix A for details). The detail coefficient matrices were absolute-valued since the averaging and differencing depend on the window structures, and in our case positive and negative contrast levels have the same meaning.

A histogram was initially calculated from each wavelet detail, measuring the frequency distribution of wavelet detail coefficients. Mean and standard deviation texture descriptors were then extracted from the histogram of each coefficient matrix, yielding six texture descriptors for every level of resolution.

Co-occurrence matrices were also calculated for each detail sub-band and level of resolution. For computational efficiency, the detail sub-bands were binned for the co-occurrence matrix to reduce the size of the matrix. The following bin sizes were investigated: 8, 16, and 64; 16 bins were found to be ideal. A

co-occurrence matrix applied to the wavelet details captures the spatial dependence of wavelet detail coefficients, depending on different directions and distances specified. A co-occurrence matrix  $C$  is an  $n \times n$  matrix, where  $n$  is the number of gray-levels within the image [1]. The matrix  $C(i, j)$  counts the number of pixel pairs having the intensities  $i$  and  $j$ . These pixel pairs are defined by specified distances and directions, which can be represented by a displacement vector  $d = (dx, dy)$ , representing the number of pixels between the pair in the  $x$  and  $y$  directions. Four co-occurrence matrices were calculated for each wavelet detail matrix at each resolution level. A co-occurrence matrix was calculated for four directions:  $0^\circ$ ,  $45^\circ$ ,  $90^\circ$ , and  $135^\circ$  at a set distance of one. Traditional co-occurrence techniques also consider several distances between pixels. However, the texture descriptors are calculated based on multi-resolution wavelets, and the resolution levels act as distances. The following nine Haralick texture descriptors were then extracted from each co-occurrence matrix: energy, entropy, contrast, homogeneity, sum-mean, variance, maximum probability, inverse difference moment, and cluster tendency [8].

Reduction of the feature vector is imperative to avoid overfitting and to obtain a manageable feature space. In general, a reduction of the number of descriptors improves the discriminative power of wavelet-based texture analysis. This hypothesis was validated by a preliminary study of the descriptor vector by a principal component analysis [24], which indicated that the most discriminative features are mean and standard deviation obtained from the histogram of detail matrices, along with contrast and maximum probability. The discriminating powers of several resolution levels as well as various feature reduction techniques were also analyzed. Initially, three levels of resolution were investigated. A feature vector averaged over co-occurrence directions (99 total features) was compared with a feature vector averaged over both co-occurrence directions and wavelet details (33 descriptors). The feature vector averaged over both co-occurrence directions and wavelet details was discovered to be ideal. The following sets of descriptors were calculated: features on individual levels of resolution (1, 2, or 3, each with only 11 descriptors), features based on two levels

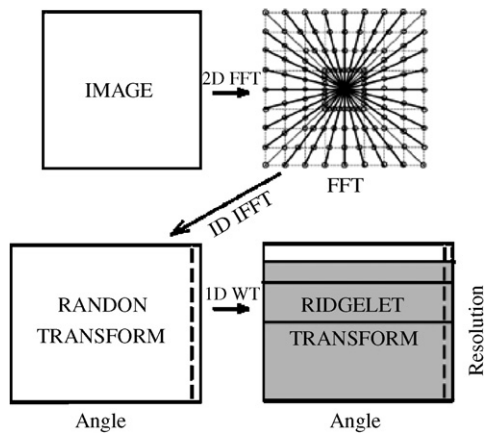


Fig. 7. Ridgelet transform flow graph.

(1 and 2, with 22 descriptors), and features based on three levels (1, 2, and 3, with 33 descriptors). The results clearly indicated that individual resolution levels did not have sufficient discriminating power, thus multiple resolutions were needed. On average, using only two levels of resolution performed better than using all three resolution levels. Thus, a feature vector of mean, standard deviation, energy, entropy, contrast, homogeneity, sum–mean, variance, cluster tendency, inverse difference moment, and maximum probability calculated from wavelet details was used for two levels of resolution resulting in 22 descriptors.

### 3.2.2. Ridgelets

The finite ridgelet transform as presented in [20], was also applied to each of the images. The ridgelet transform can be computed as illustrated in the flow chart in Fig. 7.

The ridgelet transform was computed in two steps: a calculation of a discrete radon transform and an application of a 1D wavelet transform. The radon transform was also computed in two steps: a calculation of the 2D fast Fourier transform of the image and an application of a 1D inverse Fourier transform on each of the 32 radial directions of the radon projection.

A 1D Haar wavelet was applied to each of the radial directions, for three levels of resolution. The following texture descriptors were then calculated for each radial direction and resolution level of the wavelet details: mean, standard deviation, energy, and entropy. For each level of resolution and each radial direction energy, entropy, mean, and standard deviation were calculated. The discriminating power of the following four feature vectors were investigated: energy and entropy signatures averaged over radial directions (EE), energy, entropy, mean, and standard deviation signatures averaged over radial directions (EEMS), energy signatures (Eng), and entropy signatures (Ent), neither averaged over radial directions. Each of these feature vectors was computed for three levels of resolution yielding six descriptors, 12 descriptors, and 96 descriptors, respectively.

Entropy texture descriptors were determined to yield the highest discriminating power; see Table 3 for more information. Several different combinations of resolution levels were

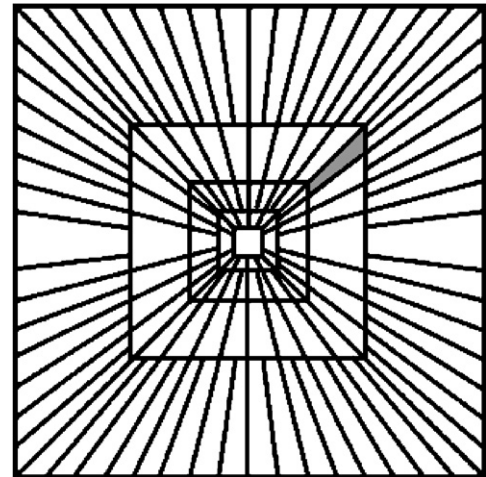


Fig. 8. Finite tiling by the polar 'wedges'.

also investigated, and two levels of resolution were determined to be best (see Ref. [7] for more details). Thus, the optimal ridgelet descriptor set yielded 64 descriptors, using two levels of resolution and entropy features from each radial direction.

### 3.2.3. Curvelets

For this paper we chose to discretize the continuous curvelet transform according to the algorithm proposed by Candes and Donoho as discussed in Ref. [22]. The discrete version implemented in this research uses a 'wrapping' algorithm. This approach uses a spatial grid to translate curvelets at each scale and angle, assuming a regular rectangular grid defining 'Cartesian' curvelets. This method applies a 2D fast Fourier transform to the image. For each scale and angle, a product of  $U_j$  is obtained (see Eq. (7)). The result is then wrapped around the origin. The 2D inverse fast Fourier transform is then applied, resulting in discrete curvelet coefficients.

The discrete curvelet transform, as presented in Ref. [16], was implemented in four steps: an application of the 2D fast Fourier transform of the image, a formation of a product of the scale and angle windows, a wrapping of this product around the origin, and an application of a 2D inverse fast Fourier transform. The discrete transform could have been calculated by sub-banding the image with wavelet decomposition and then applying a ridgelet transform, however, according to Ref. [17], the algorithm used in this paper proved to be ideal. The approximate scales and orientations can be seen in Fig. 8. Curvelets are supported by a generic 'wedge'; the shaded area provides an example of such a 'wedge'.

Several features were calculated on the curvelet coefficients. The most common statistics calculated on wavelets are mean and standard deviation. The limited literature on both curvelet-based and ridgelet-based descriptors also suggests the use of a combination of mean, standard deviation, energy, and entropy signals [11]. One of the goals of this research was to identify the most effective texture descriptors for medical images. The following three feature vectors were investigated: entropy sig-

natures (Ent), energy and entropy signatures (EE), and energy, entropy, mean, and standard deviation signatures (EEMSD). A comprehensive analysis was carried out to determine the optimal texture descriptors for the curvelet transform as applied to CT scans. Each of these statistics was calculated for three levels of resolution and for each curvelet matrix based on each radial ‘wedge’ (16 angles). This resulted in feature vectors yielding 18, 36, and 72 descriptors, respectively. The limited number of descriptors calculated on the curvelet transform generated a feature of manageable size, so no reduction was necessary.

The discrete curvelet transform can be calculated to various resolutions or scales and angles. Two parameters were involved in the digital implementation of the curvelet transform: number of resolutions and number of angles at the coarsest level. The parameters were bound by the following two constraints: the maximum number of resolutions depends on the original image size, and the number of angles at the second coarsest level must be at least eight and a multiple of four, see [16] for details. Since our images were  $32 \times 32$  pixels, the maximum possible resolution extraction was three levels of resolution. The following angles were explored: 12, 16, and 20. Using these parameters resulted in 14, 18, and 22 matrices containing structural information at three levels of resolution.

The feature vector containing energy, entropy, mean and standard deviation was determined to yield the highest discriminative power; see Table 4 for more information. The best curvelet descriptor set contained 72 descriptors, using two levels of resolution and energy, entropy, mean and standard deviation features from each ‘wedge’. Results indicated that using a feature vector containing all four curvelet-based texture descriptors significantly improved discriminatory power compared to the wavelet and ridgelet-based classification algorithms; for more details refer to [6].

### 3.3. Texture classification

The classification step was carried out using a decision tree classifier based on the C&RT approach [2]. A decision tree predicts the class of an object from values of predictor variables [1]. The most relevant texture descriptors were found for each specific organ, and based on those selected descriptors, a set of decision rules were generated. These sets of rules were then used for the classification of each region. Using the C&RT cross-validation approach, each tree’s parameter was optimized, including depth of tree, number of parent nodes, and number of child nodes. The depth of tree parameter is essentially the depth of the decision tree, and determines how much the tree will grow. The parent node is the number of possible roots per node, whereas the child node is the number of possible stems per root node. The parameters were considered optimal when the highest accuracy rate was found. To evaluate the performance of each classifier, specificity, sensitivity, precision, and accuracy rates were calculated from each of the misclassification matrices.

A misclassification matrix is a table that lists each organ and the corresponding number of true positives, true negatives, false positives, and false negatives, respectively. From the misclassification

Table 1  
Measures of classification performance

Measure	Definition
Sensitivity	True positive/total positive
Specificity	True negative/total negatives
Precision	True positive/(true positive + false positives)
Accuracy	(True positives + true negatives)/total sample

matrix specificity, sensitivity, precision, and accuracy statistics are computed (see Table 1).

Specificity measures the accuracy among positive instances; sensitivity measures the accuracy among negative instances. Precision measures show how consistently the results can be reproduced, and accuracy reflects the overall correctness of the classifier.

In the medical domain, the most important performance measures are specificity and sensitivity. Ideally, both specificity and sensitivity should be high. Theoretically, these two measures have a negative correlation. Since accuracy reflects both the sensitivity and specificity in relation to each other, this descriptor was examined to determine the overall performance of the classifier.

## 4. Results

The discriminating powers of the feature vectors are described in the following sections. Section 4.1 compares the best descriptors for Haar, Daubechies, and Coiflet wavelets. Section 4.2 compares four different feature vectors calculated on the ridgelet transform. Section 4.3 compares three different feature vectors calculated on the curvelet transform. Section 4.4 contains a global comparison of the three best multi-resolution techniques, as well as comparing them with co-occurrence and run-length-based techniques. Although some of the feature vectors contain more descriptors, it should not be assumed they would perform better than the smaller feature vectors because of the size difference. For example, it was found that a wavelet-based feature vector of 22 descriptors using two resolution levels outperformed another same-family wavelet-based feature vector of 33 descriptors using three levels of resolution. See Ref. [5] for more details.

### 4.1. Wavelet comparison

In comparing the three wavelet-based features, the Haar-based descriptors outperformed both Daubechies and Coiflet for most organs and performance measures (see Table 2).

Coiflet and Daubechies had similar performance, however Coiflet performed slightly higher with accuracy rates in the 85–93% compared to Daubechies at 83–93%. Within all the wavelets, the Haar wavelet outperformed the others in all organs with the exception of the backbone, for which the Daubechies and Coiflet wavelets produced slightly better results. This was possibly due to the fact that since the backbone has high contrasting elements, the larger windows consistently capture more

Table 2  
Performance measures of Haar, Daubechies, and Coiflet wavelets

Wavelet-based descriptors		Sensitivity	Specificity	Precision	Accuracy
Organ	Descriptor				
Backbone	Haar	82.6	96.1	82.6	93.7
	Daubechies	83.5	97.3	91.6	93.6
	Coiflet	85.9	96.8	90.7	93.1
Heart	Haar	59.0	92.1	67.0	85.0
	Daubechies	49.1	91.8	57.4	84.0
	Coiflet	67.1	89.4	58.9	85.3
Liver	Haar	77.7	91.4	69.9	88.6
	Daubechies	63.2	92.0	55.7	88.0
	Coiflet	64.3	92.2	56.7	88.3
Kidney	Haar	87.3	94.4	82.6	92.8
	Daubechies	85.4	82.9	64.9	83.6
	Coiflet	81.6	87.4	64.3	85.8
Spleen	Haar	65.5	94.3	69.7	89.5
	Daubechies	40.2	96.2	64.3	88.2
	Coiflet	35.2	97.6	70.8	88.6
Average	Haar	74.4	93.7	74.4	89.9
	Daubechies	64.2	92.0	66.8	87.5
	Coiflet	66.8	92.7	69.5	88.2

discriminating features. The Haar wavelet had in the range 59–87%, followed by Daubechies and Coiflet at 40–85% and 35–85%, respectively. The Haar wavelet also had much higher specificity ranging in 91–96% followed by Coiflet at 87–96% and Daubechies 82–97%. Precision rates followed the same pattern. The performance for the Haar-based descriptors in the majority of organs was significantly higher, thus indicating that these descriptors yield the highest discriminating power among the wavelet-based features. While more extensive testing is needed, a possible explanation for this behavior is that the texture in medical images are extremely fine. Therefore, this texture is better captured by the averaging over two adjacent pixels (Haar), rather than four (Daubechies) or six (Coiflet) adjacent pixels. Although this was not an exhaustive comparison of all possible types of wavelets, previous research studies have used these three wavelet families for comparison [14]. More importantly, ridgelet and curvelet-based texture features prove to be significantly better than wavelet-based features.

#### 4.2. Ridgelet comparison

Table 3 shows a comparison of the performance of the four ridgelet-based feature vectors based on three levels of resolution.

The entropy signatures (Ent) were in the range 91–97%, and clearly outperformed all other feature vectors. An analysis of the discriminating power of the entropy feature vector, based on the various resolution levels, was also carried out. The following sets of descriptors were calculated: Ent based on individual levels of resolution (L1, L2, and L3), Ent based on two levels (L12), and Ent based on three levels (L123). The results clearly indicated that individual resolution levels did not have sufficient

Table 3  
Performance comparison for ridgelet feature vectors

Ridgelet-based descriptors		Sensitivity	Specificity	Precision	Accuracy
Organ	Descriptor				
Backbone	Ent	90.9	98.7	93.5	97.3
	Eng	88.4	96.0	82.3	94.7
	EE	73.3	96.6	82.1	92.6
	EEMS	87.6	94.0	75.4	92.9
Heart	Ent	77.8	97.9	90.8	93.6
	Eng	56.3	95.2	76.1	86.9
	EE	44.6	87.4	49.1	78.3
	EEMS	33.2	92.6	55.0	80.0
Kidney	Ent	94.2	92.3	79.4	92.7
	Eng	93.2	88.6	72.2	89.7
	EE	72.2	86.5	56.3	83.4
	EEMS	91.7	82.7	62.7	84.9
Liver	Ent	72.5	97.7	88.5	92.7
	Eng	68.6	94.9	76.8	89.7
	EE	89.5	84.9	65.3	86.0
	EEMS	47.9	92.1	56.3	86.5
Spleen	Ent	83.8	93.4	72.9	91.7
	Eng	62.5	92.9	65.0	87.6
	EE	25.5	97.2	65.5	84.6
	EEMS	48.0	92.1	56.3	84.4
Average	Ent	83.8	96.0	85.0	93.6
	Eng	73.8	93.5	74.4	89.7
	EE	61.0	90.5	63.7	85.0
	EEMS	63.8	91.0	63.6	85.7

discriminating power, thus multiple resolutions were needed. On average, L12 performed better than L123. Table 3 contains the results for L123 on each of the four feature vectors, whereas Table 5 contains the results for L12 for Ent.

Energy (Eng) accuracy rates were significantly lower at 86–94%. The low performance of energy and entropy (EE), having 78–92% accuracy, and energy, entropy, mean, and standard deviation (EEMS), having 80–92% accuracy, indicated that averaging over directions obscures the difference in texture among organs. Averaging over directions is working against the main strength of the ridgelets, which are particularly sensitive to changes over radial directions. In comparing all other performance measures, on average, entropy outperformed all other ridgelet-based descriptors by 10–22% for specificity, 3–6% for sensitivity, 9–22% for precision, and 4–8% for accuracy.

#### 4.3. Curvelet comparison

Table 4 shows a comparison of the performance for three curvelet-based feature vectors. These results indicate that a combination of energy, entropy, mean and standard deviation (EEMSD) signatures are the most effective descriptors for curvelets.

EEMS clearly outperformed all other feature vectors, having accuracy rates between 97–98%, which was higher than both entropy (Ent) signatures (in the 91–97% range) and energy and entropy (EE) signatures (between 91–98%). EEMSD had



Table 4  
Performance comparison for curvelet feature vectors

Curvelet-based descriptors		Sensitivity	Specificity	Precision	Accuracy
Organ	Descriptor				
Backbone	EEMS	99.4	98.8	95.3	98.9
	EE	94.2	99.1	96.3	98.2
	Ent	92.7	98.7	94.4	97.5
Heart	EEMS	89.7	99.0	95.5	97.1
	EE	75.5	95.9	82.0	91.9
	Ent	74.0	96.2	82.8	91.8
Kidney	EEMS	96.0	98.1	93.5	97.6
	EE	92.3	92.1	77.1	92.2
	Ent	89.1	92.5	77.4	91.7
Liver	EEMS	95.9	98.5	94.3	98.0
	EE	81.1	97.8	90.6	94.4
	Ent	89.2	97.3	88.6	94.2
Spleen	EEMS	91.8	98.9	94.9	97.6
	EE	78.4	95.6	79.7	92.5
	Ent	80.0	94.9	77.7	94.2
Average	EEMS	94.6	98.7	94.7	97.9
	EE	84.3	96.1	85.1	93.8
	Ent	83.6	95.9	84.2	93.5

significantly higher rates for heart, liver, kidney, and spleen, which increased the accuracy by approximately 4–6%. Sensitivity rates were between 89–99% for EEMS, 75–94% for EE, and 74–92%. EEMS was significantly higher in all organs, while Ent was better than EE in liver and spleen. Specificity rates were much closer in comparison yielding results between 98–99% for EEMS, 92–99% for EE and 92–98% for Ent. The addition of Energy, Mean, and Standard Deviation signatures significantly increased performance among all organs for curvelet-based feature vectors. Considering the increased performance using the curvelet descriptors, the use of additional descriptors would be worth exploring.

#### 4.4. Global comparison

Table 5 illustrates a comparison of accuracy, precision, specificity, and sensitivity results for each tissue of interest for the best wavelet-based (Haar), best ridgelet-based (Ent), and best curvelet-based (EEMS) descriptor sets. The curvelet-based descriptors clearly outperforms all wavelet and ridgelet-based descriptors.

The ridgelet-based descriptors had significantly higher performance measures in comparison to wavelet-based descriptors, with accuracy rates 2–9% higher than any other wavelet-based feature set for all individual organs. This is not surprising given the fact that the ridgelet transform is able to capture multi-directional features, as opposed to the wavelet transform which focus mainly on horizontal, vertical, and diagonal features, which are not dominant in medical CT scan images. Curvelet-based descriptors had an even higher performance in comparison to both the wavelet and ridgelet, with accuracy rates approximately 5–12% and 1–4% higher, respec-

Table 5  
Comparison of the best wavelet-based (Haar), ridgelet-based (entropy), and curvelet-based (EEMSD) descriptors

Organ	Descriptor	Sensitivity	Specificity	Precision	Accuracy
Backbone	Curvelet	99.4	98.8	95.3	98.9
	Ridgelet	91.5	99.3	96.8	98.0
	Wavelet	82.6	96.1	82.6	93.7
Heart	Curvelet	89.7	99.0	95.5	97.1
	Ridgelet	82.5	97.5	88.5	94.6
	Wavelet	59.0	92.1	67.0	85.0
Kidney	Curvelet	96.0	98.1	93.5	97.6
	Ridgelet	95.4	93.3	82.0	93.8
	Wavelet	77.7	91.4	69.9	88.6
Liver	Curvelet	95.9	98.5	94.3	98.0
	Ridgelet	86.9	95.9	84.4	94.0
	Wavelet	87.3	94.4	82.6	92.8
Spleen	Curvelet	91.8	98.9	94.9	97.6
	Ridgelet	76.9	97.6	88.0	93.8
	Wavelet	65.5	94.3	69.7	89.5
Average	Curvelet	94.6	98.7	94.7	97.9
	Ridgelet	86.6	96.7	88.0	94.8
	Wavelet	74.4	93.7	74.4	89.9

tively. Curvelet-based features yielded accuracy rates between 97% and 98%, which significantly improved accuracy ranges for ridgelet-based features and wavelet-based features. Accuracy rates for wavelet-based texture descriptors ranged between 85–93%, while ridgelet-based descriptors were 93–98%, and curvelet-based accuracy rates were in the 97–98% range. This was also expected since the curvelet transform is able to capture multi-directional features in wedges, as opposed to lines or points as in the ridgelet or wavelet transform. The multi-directional features in curvelets prove to be very effective in the texture classification of the more organic textures in medical images.

The curvelet-based algorithm was also compared to two other non-wavelet-based texture classification algorithms, co-occurrence and run-length. Although ridgelet-based and wavelet-based features performed lower than co-occurrence and run-length, the curvelet-based features had a higher discriminating power than both co-occurrence and run-length in all organs as shown in Table 6. The curvelet-based algorithm had accuracy rates in the 97–98% range, compared to co-occurrence-based algorithm with 94–97% and run-length-based algorithm with 91–98% accuracy. Sensitivity rates were highest among the curvelet-based descriptors with 91–99% as compared to co-occurrence and run-length at 84–91% and 71–93%, respectively. Specificity rates yielded between 98–99% for the curvelet-based descriptors set. This was also better than the co-occurrence descriptor set which yielded 96–98% and run-length which resulted in 94–98%. Precision was also highest with the curvelet descriptors with 93–95% as compared to 87–94% and 82–95% from the co-occurrence and run-length descriptor sets, respectively. The curvelet-based algorithm has significantly improved upon previous texture

Table 6  
Comparison of the curvelet-based, co-occurrence, and run-length descriptors

Organ	Descriptor	Sensitivity	Specificity	Precision	Accuracy
Backbone	Curvelet	99.4	98.8	95.3	98.9
	Co-occurrence	91.8	98.9	94.6	97.6
	Run-length	93.9	98.8	95.7	98.0
Heart	Curvelet	89.7	99.0	95.5	97.1
	Co-occurrence	84.8	96.6	87.2	94.1
	Run-length	71.1	96.5	83.1	91.5
Kidney	Curvelet	96.0	98.1	93.5	97.6
	Co-occurrence	97.8	96.0	88.7	96.5
	Run-length	92.1	94.7	83.3	94.1
Liver	Curvelet	95.9	98.5	94.3	98.0
	Co-occurrence	86.5	97.4	89.3	95.3
	Run-length	89.8	94.6	82.0	93.9
Spleen	Curvelet	91.8	98.9	94.9	97.6
	Co-occurrence	84.7	97.7	88.6	95.4
	Run-length	74.3	95.7	79.1	91.8
Average	Curvelet	94.6	98.7	94.7	97.9
	Co-occurrence	89.1	97.3	89.7	95.8
	Run-length	84.3	96.1	84.7	93.9

classification algorithms. The algorithm presented in this article is able to classify normal tissues in CT scans with high accuracy rates. The data set is limited and these hypotheses should be further tested and validated on different data sets. These results are promising, and applications to other data sets are currently being explored.

## 5. Summary

The research presented in this article is aimed at the development of an automated imaging system for classification of tissues in medical images obtained from computed tomography (CT) scans. Classification of human organs in CT scans using shape or gray-level information proves to be a particularly challenging task. This is due primarily to the changing shape of organs in a stack of slices in 3D medical images and the gray-level intensity overlap in soft tissues. Even so, healthy organs are expected to have a consistent texture within tissues across multiple slices. Therefore, texture analysis of CT scans can be used for the classification or segmentation of images based on these textural variations of intensity. This research focuses on using multi-resolution texture analysis for the classification of tissues from normal chest and abdomen CT scans. It offers a comprehensive analysis of texture classification algorithms using five sets of wavelet, ridgelet, and curvelet-based texture vectors,

as well as a comparison with two standard texture classification algorithms based on co-occurrence and run-length based texture vectors. Features for the five texture vectors were extracted from the following transforms: the Haar wavelet, Daubechies wavelet, Coiflet wavelet, a ridgelet, and a curvelet.

The texture classification algorithm proposed in this article consists of three main steps: segmentation of regions of interest from CT scans, extraction of the most discriminative texture features, and creation of a classifier that automatically identifies the various organs. The overall goal is to develop a textural model for each texture class in the data set. The initial segmentation is obtained using a supervised Active Contour Model algorithm, and the classification step is carried out using a C&RT with cross-validation. Tests comparing the wavelet, ridgelet, and curvelet texture features indicated that curvelet-based signatures outperform all other multi-resolution techniques, yielding accuracy rates in the 97–98% range. In comparison, a similar algorithm based on wavelet yielded accuracy rates in the 85–93% range at best, and the algorithm based on ridgelet texture descriptors yielded accuracy rates in the 91–97% range. The paper also compares these multi-resolution techniques with standard co-occurrence and run-length-based texture classification algorithms. Tests indicate that the curvelet-based algorithm outperformed both the co-occurrence and the run-length algorithm by 1–2% in accuracy rates for each tissue of interest. These results clearly indicate that using curvelet-based texture features significantly improved the classification of normal tissues in CT scans. The authors are currently validating these results against several new sets of data obtained from different patients and different CT scanner as well as comparing the accuracy of the classifier against expert-labeled tissues.

## Acknowledgements

This work was supported in parts by the National Science Foundation under Grant No. 0453456. This work was completed in conjunction with Northwestern Memorial Hospital, DePaul University's MedIX program and DePaul University's Intelligent Multi-media Processing Laboratory. The authors would like to thank Dr. David Channin, MD, Northwestern Memorial Hospital, Dr. Jacob Furst, Dr. Daniela Raicu, DePaul University, and William Brandon Kerr, Trinity University, for their valuable comments and feedback throughout this project.

## Appendix A. Feature equations [1]

Feature	Formula	What is measured?
Entropy	$-\sum_i^M \sum_j^N P[i, j] \log P[i, j]$	Measures the randomness of a gray-level distribution. The entropy is expected to be high if the gray levels are distributed randomly throughout the image

Energy (angular second moment)	$\sum_i^M \sum_j^N P^2[i, j]$	Measures the number of repeated pairs. The energy is expected to be high if the occurrence of repeated pixel pairs is high
Contrast	$\sum_i^M \sum_j^N (i - j)^2 P[i, j]$	Measures the local contrast of an image. The contrast is expected to be low if the gray levels of each pixel pair are similar
Homogeneity	$\sum_i^M \sum_j^N \frac{P[i, j]}{1 +  i - j }$	Measures the local homogeneity of a pixel pair. The homogeneity is expected to be large if the gray levels of each pixel pair are similar
Sum–mean (mean)	$\frac{1}{2} \sum_i^M \sum_j^N (i P[i, j] + j P[i, j])$	Provides the mean of the gray levels in the image. The sum–mean is expected to be large if the sum of the gray levels of the image is high
Variance	$\frac{1}{2} \sum_i^M \sum_j^N ((i - \mu)^2 P[i, j] + (j - \mu)^2 P[i, j])$	Variance tells us how spread out the distribution of gray levels is. The variance is expected to be large if the gray levels of the image are spread out greatly
Maximum probability (MP)	$\text{Max}_{i,j}^{M,N} P[i, j]$	Results in the pixel pair that is most predominant in the image. The MP is expected to be high if the occurrence of the most predominant pixel pair is high
Inverse difference moment (IDM)	$\sum_i^M \sum_j^N \frac{P[i, j]}{ i - j ^k}, \quad i \neq j$	Inverse difference moment tells us about the smoothness of the image, like homogeneity. The IDM is expected to be high if the gray levels of the pixel pairs are similar
Cluster tendency	$\sum_i^M \sum_j^N (i + j - 2\mu)^k P[i, j]$	Measures the grouping of pixels that have similar gray level values

## Appendix B. General filtering structure

$$\begin{bmatrix} h_2 & h_3 & h_4 & h_5 & 0 & 0 & 0 & 0 & h_0 & h_1 \\ g_2 & g_3 & g_4 & g_5 & 0 & 0 & 0 & 0 & g_0 & g_1 \\ h_0 & h_1 & h_2 & h_3 & h_4 & h_5 & 0 & 0 & 0 & 0 \\ g_0 & g_1 & g_2 & g_3 & g_4 & g_5 & 0 & 0 & 0 & 0 \\ 0 & 0 & h_0 & h_1 & h_2 & h_3 & h_4 & h_5 & 0 & 0 \\ 0 & 0 & g_0 & g_1 & g_2 & g_3 & g_4 & g_5 & 0 & 0 \\ 0 & 0 & 0 & 0 & h_0 & h_1 & h_2 & h_3 & h_4 & h_5 \\ 0 & 0 & 0 & 0 & g_0 & g_1 & g_2 & g_3 & g_4 & g_5 \\ h_4 & h_5 & 0 & 0 & 0 & 0 & h_0 & h_1 & h_2 & h_3 \\ g_4 & g_5 & 0 & 0 & 0 & 0 & g_0 & g_1 & g_2 & g_3 \end{bmatrix}$$

**Appendix C. Haar, Daubechies, and Coiflet scaling and wavelet function coefficients**

Scaling	$h_0$	$h_1$	$h_2$	$h_3$	$h_4$	$h_5$
Haar	$\frac{1}{\sqrt{2}}$	$\frac{1}{\sqrt{2}}$				
Daubechies	$\frac{1+\sqrt{3}}{4*\sqrt{2}}$	$\frac{3+\sqrt{3}}{4*\sqrt{2}}$	$\frac{3-\sqrt{3}}{4*\sqrt{2}}$	$\frac{1-\sqrt{3}}{4*\sqrt{2}}$		
Coiflet	$\frac{1-\sqrt{7}}{16*\sqrt{2}}$	$\frac{5+\sqrt{7}}{16*\sqrt{2}}$	$\frac{14+2\sqrt{7}}{16*\sqrt{2}}$	$\frac{14-2\sqrt{7}}{16*\sqrt{2}}$	$\frac{1-\sqrt{7}}{16*\sqrt{2}}$	$\frac{-3+\sqrt{7}}{16*\sqrt{2}}$
Wavelet	$g_0$	$g_1$	$g_2$	$g_3$	$g_4$	$g_5$
Haar	$\frac{1}{\sqrt{2}}$	$-\frac{1}{\sqrt{2}}$				
Daubechies	$\frac{1-\sqrt{3}}{4*\sqrt{2}}$	$\frac{-3-\sqrt{3}}{4*\sqrt{2}}$	$\frac{3+\sqrt{3}}{4*\sqrt{2}}$	$\frac{-1-\sqrt{3}}{4*\sqrt{2}}$		
Coiflet	$\frac{-3+\sqrt{7}}{16*\sqrt{2}}$	$\frac{-1+\sqrt{7}}{16*\sqrt{2}}$	$\frac{14-2\sqrt{7}}{16*\sqrt{2}}$	$\frac{-14-2\sqrt{7}}{16*\sqrt{2}}$	$\frac{5+\sqrt{7}}{16*\sqrt{2}}$	$\frac{-1+\sqrt{7}}{16*\sqrt{2}}$

**References**

- [1] D.H. Xu, J. Lee, D.S. Raicu, J.D. Furst, D. Channin, Texture classification of normal tissues in computed tomography, The 2005 Annual Meeting of the Society for Computer Applications in Radiology, Orlando, FL, USA, 2005.
- [2] D. Channin, D.S. Raicu, J.D. Furst, D.H. Xu, L. Lilly, C. Limsangsri, Classification of tissues in computed tomography using decision trees, The 90th Scientific Assembly and Annual Meeting of Radiology Society of North America, 2004.
- [3] A. Kurani, D.H. Xu, J.D. Furst, D.S. Raicu, Co-occurrence matrices for volumetric data, in: The Seventh IASTED International Conference on Computer Graphics and Imaging—CGIM 2004, Kauai, Hawaii, USA, 2004, pp. 426–443.
- [4] D.H. Xu, A. Kurani, J.D. Furst, D.S. Raicu, Run-length encoding for volumetric texture, The Fourth IASTED International Conference on Visualization, Imaging, and Image Processing—VIIP 2004, Marbella, Spain, 2004, pp. 452–458.
- [5] L. Semler, L. Dettori, J. Furst, Wavelet-based texture classification of tissues in computed tomography, in: Proceedings of the 18th IEEE International Symposium on Computer-Based Medical Systems, Dublin, Ireland, 2005, pp. 265–270.
- [6] L. Semler, L. Dettori, Curvelet-based texture classification in computed tomography, International Conference on Image Processing, Atlanta, GA, USA, 2006.
- [7] L. Semler, L. Dettori, A comparison of wavelet-based and ridgelet-based texture classification of tissues in computed tomography, in: Proceedings of International Conference on Computer Vision Theory and Applications, 2006, pp. 285–289.
- [8] R.M. Haralick, L.G. Shapiro, Computer and Robot Vision, Addison-Wesley Publishing Co., Boston, MA, USA, 1992.
- [9] S. Handrick, B. Naimipour, J.D. Furst, D.S. Raicu, Binning strategies evaluation for tissue classification in computed tomography images, in: Proceedings of SPIE Medical Imaging Conference, vol. 6144, San Diego, CA, 2006, pp. 1476–1486.
- [10] B. Kara, N. Watsuji, Using wavelets for texture classification, in: IJCI Proceedings of International Conference on Signal Processing, ISN 1304-2386, 2003, pp. 920–924.
- [11] H.L. LeBorgne, N. O'Connor, Natural scene classification and retrieval using ridgelet-based image signatures, Adv. Concepts Intell. Vision Syst. (2005) 20–23.
- [12] J.L. Starck, D.L. Donoho, E.J. Candes, Astronomical image representation by the curvelet transform, Astron. Astrophys. 398 (1999) 785–800.
- [13] E. Stollnitz, T. DeRose, D. Salesin, D. Wavelets for computer graphics: a primer part 1, IEEE Comput. Graph. Appl. 15 (3) (1995) 76–84.
- [14] S. Rajeev, R.E. Vasquez, R. Singh, Comparison of Daubechies, Coiflet, and Symlet for edge detection, Visual Information Processing VI, vol. 3074, SPIE, 1997, pp. 151–159.
- [15] D. Donoho, Ridge functions and orthonormal ridgelets, J. Approx. Theory 111 (2) (2001) 143–179.
- [16] E. Candes, L. Demanet, D. Donoho, L. Ying, Fast discrete curvelet transforms, SIAM Multiscale Modeling Simul. (2006).
- [17] J.L. Starck, M. Elad, D. Donoho, Redundant multiscale transforms and their application for morphological component separation, Adv. Imaging Electron Phys. 132 (2004) 287–348.
- [18] C. Mulcahy, Image compression using the Haar wavelet transform, Spelman Sci. Math J. 1 (1997) 22–31.
- [19] W. Fourati, F. Kammoun, M.S. Bouhlel, Medical image denoising using wavelet thresholding, J. Test. Eval. 33 (5) (2005).
- [20] M.N. Do, M. Vetterli, The finite ridgelet transform for image representation, IEEE Trans. Image Process. 12 (2003) 16–28.
- [21] J. Li, A wavelet approach to edge detection, Master of Science Thesis, Sam Houston State University, Huntsville, TX, 1993.
- [22] E.J. Candes, D.L. Donoho, Curvelets, multi-resolution representation, and scaling laws, Wavelet Applications in Signal and Image Processing VIII, vol. 4119-01, SPIE, 2000.
- [23] A. Jensen, A. Cour-Harbo, Ripples in Mathematics: The Discrete Wavelet Transform, first ed., Springer, Berlin, 2001, ISBN: 3540416625.
- [24] L. Smith, A Tutorial on Principal Components Analysis, [www.cs.otago.ac.nz/cosc453/student\\_tutorials/principal\\_components.pdf](http://www.cs.otago.ac.nz/cosc453/student_tutorials/principal_components.pdf), 2002.
- [25] A. Mojsilovic, M. Popovic, S. Markovic, M. Krstic, Characterization of visually similar diffuse diseases from B-scan liver images using nonseparable wavelet transform, IEEE Trans. Med. Imaging 17 (4) (1998) 541–549.
- [26] B.S. Manjunath, P. Wu, S. Newsam, H.D. Shin, A texture descriptor for browsing and similarity retrieval, Signal Process.: Image Commun. 16 (1) (2000) 33–43.
- [27] M. Do, M. Vetterli, Image denoising using orthonormal finite ridgelet transform, in: Proceedings of SPIE: Wavelet Applications in Signal and Image Processing, vol. 4119, 2003, pp. 831–842.



**Lucia Dettori** graduated from the University of Paris XI (Paris, France) in 1994 with a Ph.D. in Applied Mathematics. She has held Visiting Assistant Professor positions at Brown University and Southern Methodist University. She is currently an Assistant Professor in the School of Computer Science, Telecommunications, and Information Systems at DePaul University (Chicago, USA). Her research interests include medical image processing, scientific computing, numerical solutions of partial differential equations using spectral methods, and Computer Science education.

**Lindsay Semler** graduated from DePaul University (Chicago, USA) in 2006 with a Bachelors of Science in Computer Graphics and Animation. She is currently pursuing a Masters degree in Software Engineering at DePaul University. Her research involves texture classification of tissues in computed tomography and image processing using multi-resolution analysis such as Wavelets, Ridgelets, and Curvelets.